Available online at www.keaipublishing.com/en/journals/journal-of-magnesium-and-alloys/

ScienceDirect

Journal of Magnesium and Alloys 13 (2025) 1523–1535

www.elsevier.com/locate/jma

Full Length Article

Degradation behavior of pure Mg in the physiological medium and growth mechanism of surface corrosion product films

Chenyu Wang[a], Mingshan Sun[b], Chao Yang[a,*], Haiyang Wang[a], Jie Wang[a], Lin Mao[c], Yao Yang[a], Tao Ying[a], Paul K. Chu[d], Xiaoqin Zeng[a,*]

[a] *National Engineering Research Center of Light Alloy Net Forming, School of Materials Science and Engineering, Shanghai Jiao Tong University, Shanghai 200240, China*

[b] *Kunming Branch of the 705 Research Institute of CSSC, Kunming 650101, China*

[c] *Shanghai Institute for Minimally Invasive Therapy, School of Medical Instrument and Food Engineering, University of Shanghai for Science and Technology, Shanghai 200093, China*

[d] *Department of Physics, Department of Materials Science & Engineering, and Department of Biomedical Engineering, City University of Hong Kong, Tat Chee Avenue, Kowloon, Hong Kong, China*

Received 13 March 2024; received in revised form 6 May 2024; accepted 16 May 2024
Available online 25 July 2024

Abstract

Pure Mg boasting a relatively small corrosion rate is a potential biodegradable metal material for implants. However, its degradation behavior in the complex physiological environment is still a lack of understanding. In this work, we investigated the effect of corrosion product film layers on the degradation behavior of pure Mg in physiological environments. Pure Mg shows a faster corrosion rate in simulated body fluid (SBF) compared to NaCl solution. Hydrogen evolution experiments indicate that the degradation rate of pure Mg in SBF decreases rapidly within the first 12 h but stabilizes afterward. The rapid deposition of low-solubility calcium phosphate on the pure Mg in SBF provides protection to the substrate, resulting in a gradual decrease in the degradation rates. Consequently, the corrosion product film of pure Mg formed in SBF exhibits a layered structure, with the upper layer consisting of dense $Ca_3(PO_4)_2/Mg_3(PO_4)_2$ and the lower layer consisting of $Mg(OH)_2/MgO$. Electrochemical impedance spectroscopy (EIS) shows that the resistance of the corrosion product film increases over time, indicating gradual strengthening of the corrosion resistance. The 4-week degradation results in the femoral marrow cavity of mice are consistent with the result in SBF *in vitro*.

Keywords: Pure Mg; Physiological environment; Degradation behavior; Corrosion product film; Calcium phosphate.

1. Introduction

In recent years, implantable medical metals with excellent mechanical properties have been used in bone repair, anti-tumor and disease therapies [1–4]. In bone repair and engineering, stainless steel and titanium alloys are predominantly utilized clinically, but they have drawbacks such as high elastic modulus and non-degradability, which can result in stress shielding and necessitate second surgeries in case of infections [5–8]. In contrast, biodegradable metals that offer multiple functions degrade gradually after implantation and do not require a second surgery [9–11]. In particular, Mg stands out due to its low density, lightweight, high specific strength as well as complete degradation *in vivo* [4,6,12,13]. Additionally, Mg^{2+} produced during Mg degradation can facilitate the proliferation and differentiation of bone cells and plays a crucial role in the growth of bone cells and nervous and cardiac systems. In addition, H_2 released during degradation can inhibit the growth of tumor cells, making it valuable in bone repair, vascular stents, and anti-tumor treatment [14–17].

* Corresponding authors.
E-mail addresses: chaoyang0315@163.com (C. Yang), xqzeng@sjtu.edu.cn (X. Zeng).

https://doi.org/10.1016/j.jma.2024.05.012

Until now, most medical applications of Mg have focused on Mg alloys because of the better mechanical properties for load-bearing applications [18–21]. However, most Mg alloys usually have poor corrosion resistance in the physiological environment, and the rapid degradation rate can lead to a highly alkaline environment and excessive hydrogen gas production, thereby impeding tissue regeneration [22,23]. There are two main reasons for the rapid degradation of Mg alloys: (1) They have low standard electrode potentials (pure Mg is −2.37 V) and are thus prone to galvanic corrosion with the second phase and (2) The surface oxide films on Mg alloys are loose and cannot play the protective effect of passivation layers [24–26]. Currently, rare earth alloying has been shown in research to reduce corrosion rates to very low levels [27–30]. For instance, Zeng et al. [30] developed a novel Mg-Y-Al alloy with high strength and excellent corrosion resistance, achieving a corrosion rate below 0.2 $mm \cdot y^{-1}$. However, most high corrosion-resistant Mg alloys currently incorporate aluminum and rare earth elements, which, unfortunately, pose certain hazards to human health [31,32]. Surface coatings can reduce the degradation rates of Mg alloys, but if the surface coatings are broken through, rapid degradation can lead to health problems [33–36].

In contrast, pure Mg with high purity (more than 99.99%) can avoid galvanic corrosion caused by impurities because of the low corrosion rate. Actually, there is a wealth of research on the degradation performance of pure magnesium [37–41]. For example, Hong et al. [37] studied the effect of grain size on the corrosion rate of pure Mg and found only a weak effect. Ren et al. [40] found that reducing impurity elements and refining grain size in pure Mg can slow down its corrosion rate in physiological solution. Bland et al. [41] demonstrated that the thickness of the oxide film on pure Mg exhibits a clear dependence on crystal orientation. However, the grain size and orientation of pure Mg have little effect on its degradation rate and remain within a relatively low range. It has recently been used for non-weight-bearing applications such as femoral condyle and other parts [42–45]. Huang et al. [46] have implanted pure Mg rods into the femur of Japanese white rabbits, and found that the degradation process is relatively slow and shows good biological safety. At the same time, the new bone-like tissues around the Mg rods form rapidly, giving rise to good bone induction. Miao et al. [47] have implanted pure Mg into the femur of rabbits and removed the femoral shaft after 4 weeks, and scanning electron microscopy (SEM) and cone beam CT (CBCT) indicate that the changes around pure Mg are consistent with the healing process of normal bone. Several studies have shown that pure Mg has acceptable degradation rates *in vivo* and can promote bone repair in non-weight-bearing applications.

However, the degradation behavior of pure Mg in physiological environments is still unclear. Some researchers found that the corrosion rate of pure Mg increases in physiological solutions, while others suggest that the corrosion rate is slower than that of salt solution [48–50]. This differentiation is due to the higher composition of anions in physiological environments, including Cl^-, HCO_3^-, HPO_4^{2-} and $H_2PO_4^-$, making the corrosion behavior of pure Mg more complex [51]. Typically, the changes in corrosion rate of pure Mg in physiological environments are related to its corrosion kinetics, and the corrosion product film formed will affect this process [51]. This has been more widely studied in the corrosion behavior of multi-element Mg alloys, where constructing a structurally dense corrosion product film can reduce the corrosion rate, while a loose structure will accelerate corrosion [52–54]. However, due to the single composition of pure Mg, the impact of its corrosion product film on corrosion is easily overlooked. In fact, in addition to hydroxides, the corrosion product film in physiological environments may also include easily deposited phosphates, carbonates, etc. [51]. Therefore, it is crucial to study the degradation behavior of pure Mg in physiological environments from the perspective of corrosion products.

In this study, the degradation behavior of pure Mg in SBF and NaCl solution is compared systematically by immersion and hydrogen evolution experiments. The corrosion products on the surface and cross-section of pure Mg after immersion for 168 h are characterized. The structure and composition of the corrosion products and the evolution of the corrosion product film are studied. The electrochemical properties of pure Mg in SBF are determined to evaluate the passivation behavior and degradation mechanism. The results are compared to those observed in mice *in vivo*.

2. Experimental details

2.1. Degradation tests

The polished pure Mg (99.99%, cast state, The microstrucure were characterized in Fig. S1) with dimensions of 20 × 20 × 5 mm^3 were immersed in the 3.5 wt.% NaCl solution and SBF for 168 h at 37 °C to test the weight loss and hydrogen evolution. Each experiment was conducted three times to obtain averages. The hydrogen evolution data were recorded every 2 h in the first 12 h and followed by recordings every 12 h thereafter. After immersion for 168 h, the corrosion products were cleaned for 3 min with a solution of 200 $g \cdot L^{-1}$ CrO_3 and 10 $g \cdot L^{-1}$ $AgNO_3$ in the weight loss experiment. The corrosion rate due to weight loss was calculated by the following formula:

$$P_W = 2.10W, \tag{1}$$

where W is the weight loss rate (in $mg \cdot cm^{-2} \cdot day^{-1}$) and P_W is the corrosion rate from weight loss (in $mm \cdot y^{-1}$). The hydrogen evolution rate at each time was calculated by the following formula (2).

$$HER_n = \frac{HEV_n - HEV_{n-1}}{T_n - T_{n-1}}, \tag{2}$$

where *HER* is the hydrogen evolution rate at time (in $mL \cdot cm^{-2} \cdot day^{-1}$), *HEV* is the hydrogen evolution volume (in $mL \cdot cm^{-2}$) and T is the time (in day).

2.2. Electrochemical assessment

The Tafel curves and electrochemical impedance spectroscopy (EIS) data were obtained from the pure Mg samples at 37 °C in 3.5 wt.% NaCl and SBF on the Gamry 1010E electrochemical workstation. A standard three-electrode system with a saturated calomel electrode (SCE) as the reference electrode, platinum electrode as the counter electrode, and the sample as the working electrode was employed. Before each test, the sample was immersed in the solution for 1 h to achieve a stable open circuit potential (OCP). The Tafel tests were conducted in the range from EOCP − 0.4 V to EOCP + 0.8 V at a scanning rate of 1 $mV{\cdot}s^{-1}$. EIS was performed at OCP in the frequency range between 100 kHz to 10 mHz with a perturbation of 10 mV. The EIS results were analyzed by the ZSimpWin software. To ensure the reproducibility of the electrochemical results, each test was repeated at least three times.

2.3. Microstructure characterization

The pure Mg was polished (MECATECH 334, PRESI) before conducting electron backscattering diffraction (EBSD, Oxford AZtec EBSD system) to examine the grain structure. The microstructure and corrosion morphology after corrosion in 3.5 wt.% NaCl and SBF were observed by scanning electron microscopy (SEM, RISE-MAGNA, TESCAN), and the elemental composition was determined by energy-dispersive X-ray spectroscopy (EDS, Oxford AZtec X-MaxN 80). A Cu target ($\lambda = 0.15418$ nm) was used as the X-ray source, and the structure was determined by X-ray diffraction (XRD, Bruker, D8 Advance). The composition of the corrosion products was determined by grazing incidence X-ray diffraction (GIXRD, Aeris, Malvern Panaalytical) using a scanning rate of $5°{\cdot}min^{-1}$, step size of 0.05 s, and 2θ range from 10° to 80°. The elemental composition of the degradation products was determined by X-ray photoelectron spectroscopy (XPS, NEXSA, Thermo Fisher Scientific), and the binding energy was referenced to the C 1s peak (284.8 eV). The spectra were fitted by the Avantage 5.978 software.

2.4. Cell cytotoxicity test

The human umbilical vein immortalized endothelial cells (HUVEC) were cultured in a cell culture incubator (37 °C, 5% CO_2 concentration, saturated humidity, sterile) with the complete culture medium (ratio: high glucose DMEM+10% high-grade fetal bovine serum SFBS+1% penicillin/streptomycin antibiotic P/S). The sample extraction solution was prepared according to the ISO 10,993–12:2002 standard. To prepare the 100% extraction solution, SFBS and P/S were added in proportion to the complete growth medium. Diluted solutions of 10% (1 vol of 100% extraction solution + 9 vol of complete growth medium) and 50% (5 vol of 100% extraction solution + 5 vol of complete growth medium) were prepared using the complete growth medium and 100% extraction solution. The cell viability was assessed using the CCK-8 assay.

2.5. Degradation in mice in vivo

Three 6-week-old male mice weighing between 120 and 150 g were used to create a femoral intramedullary implant model. After the mice were anesthetized, a pure magnesium cylindrical rod 10 mm long and 1 mm in diameter was implanted in the femur. After surgery, the mice were monitored until they could move freely and were then individually housed in cages. Subcutaneous injections of sodium penicillin (15 $mg{\cdot}kg^{-1}$ body weight) were administered for three consecutive days after the operation. One month later, samples were taken at the femoral condyle for SEM and EDS photography to obtain corrosion morphology and element distribution information. All animal studies/procedures have been approved by Ethics Committee (20230410(7)) and performed in accordance with the ethical standards.

3. Results and discussion

Fig. 1 shows the degradation rates of pure Mg in 3.5 wt.% NaCl and SBF at 37 °C. Fig. 1a displays the calculated weight loss of pure Mg after immersion in the solution for 168 h. The corrosion rate in 3.5 wt.% NaCl at 37 °C is 0.60 $mm{\cdot}y^{-1}$, which is higher than the average corrosion rate of pure Mg in the NaCl solution at room temperature (0.2–0.3 $mm{\cdot}y^{-1}$). This is because a higher temperature accelerates corrosion. In comparison, the corrosion rate of pure Mg in SBF is 2.81 $mm{\cdot}y^{-1}$, which is significantly higher than that in the NaCl solution. In addition, this rate is slower than the corrosion rate of typical Mg alloys [55–57], therefore, pure Mg exhibits better potential in physiological environments. The results of hydrogen evolution after 168 h in Fig. 1b are consistent with the weight losses. The amount of hydrogen emitted from the pure Mg in SBF after 168 h is 13.82 $mL{\cdot}cm^{-2}$, which is larger than 1.86 $mL{\cdot}cm^{-2}$ from the NaCl solution, suggesting that degradation is faster in SBF due to the more complex anionic environment. In the corrosive alkaline environment, HCO_3^- and $H_2PO_4^-/HPO_4^{2-}$ lose H to generate more H_2, thus accelerating the conversion of elemental Mg to Mg^{2+}. Consequently, the degradation of pure Mg becomes more severe in SBF.

Fig. 1c shows the H_2 evolution rates from the pure Mg in SBF and NaCl solution at various time intervals. The decreasing trend in the H_2 evolution rate in both liquids can be attributed to the formation of a corrosion product film on the pure Mg during corrosion, which provides a certain level of protection against corrosion. After immersion in the NaCl solution for 12 h, the hydrogen evolution rate of pure Mg stabilizes to 0.36 $mL{\cdot}cm^{-2}{\cdot}day^{-1}$. The hydrogen evolution rate of pure Mg in the early stage of immersion in SBF is relatively high at 15.28 $mL{\cdot}cm^{-2}{\cdot}day^{-1}$ after 2 h, indicating accelerated corrosion in SBF. However, it decreases rapidly to 3.62 $mL{\cdot}cm^{-2}{\cdot}day^{-1}$ within 12 h and further diminishes to 1.82 $mL{\cdot}cm^{-2}{\cdot}day^{-1}$ after 72 h before stabilizing (Fig. 1d). As corrosion progresses, the corrosion product layer thickens gradually to provide more protection. Consequently, the hydrogen evolution rates in NaCl and SBF continue to de-

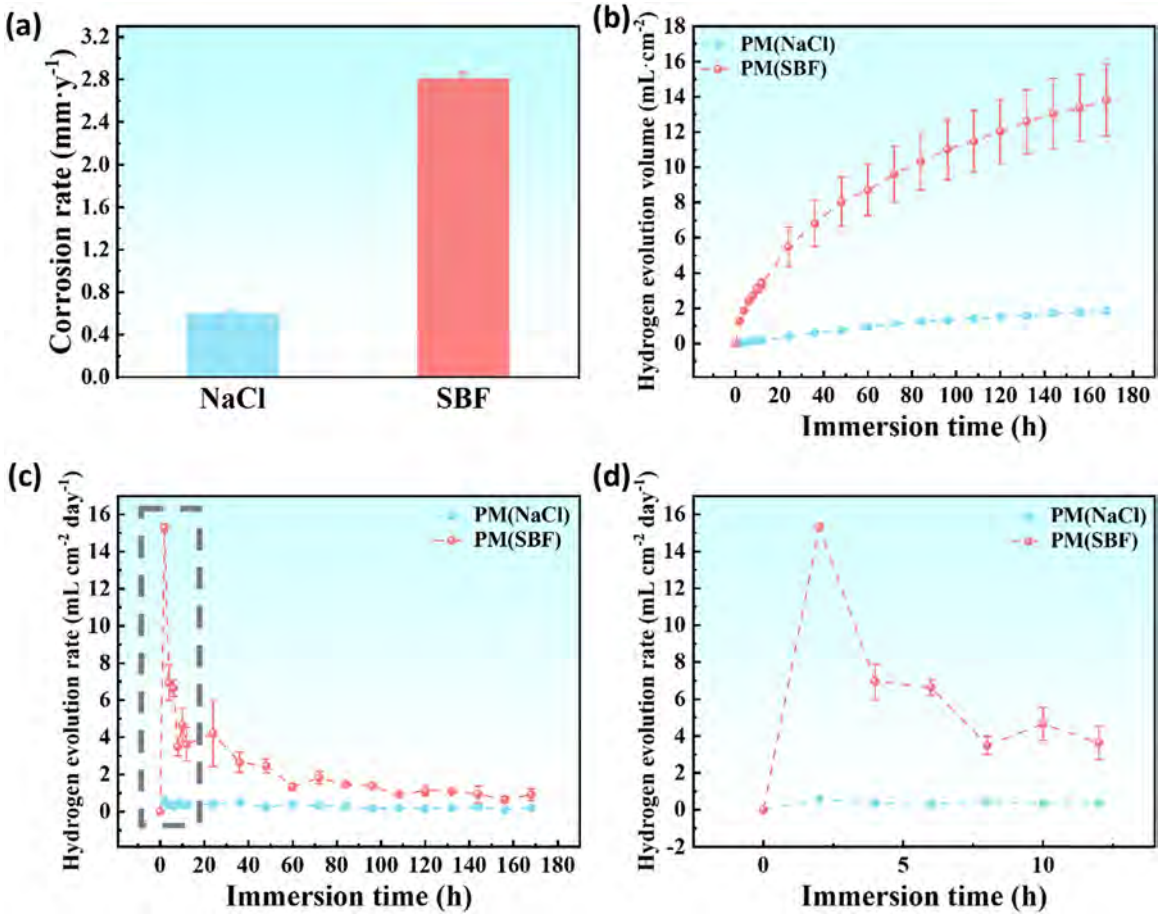

Fig. 1. Corrosion degradation of pure Mg in SBF and NaCl solution: (a) Weight loss corrosion rate; (b) Hydrogen evolution volume and (c, d) Hydrogen evolution rate.

crease at a slower rate, reaching 0.19 mL·cm^{-2}·day $^{-1}$ and 0.91 mL·cm^{-2}·day $^{-1}$, respectively after 168 h. Despite the significant disparity in the hydrogen evolution rates at the onset of corrosion (SBF being 26 times higher than the NaCl solution), the rate in SBF after 168 h is only 4.67 times higher than that in the NaCl solution. This change may be influenced by the corrosion product film. In addition, it is worth noting that pH levels can indeed influence the corrosion rate of Mg and Mg alloys [58,59]. Especially in salt solution, an increase in pH tends to stabilize magnesium hydroxide, resulting in a slower corrosion rate [60]. However, in SBF, the presence of buffering agents maintains a relatively stable pH during alloy degradation [61], therefore, we did not discuss in detail the effect of pH on the degradation process.

Fig. 2 shows the surface morphology and elemental composition distribution of pure Mg after immersion in the NaCl solution and SBF for 168 h. The pure Mg shows a loose and porous corrosion product film on the surface after immersion in the NaCl solution for 168 h (Fig. 2a). EDS shows that the corrosion product film is mainly composed of Mg and O, indicative of $Mg(OH)_2$ and MgO. In contrast, the corrosion product film on the pure Mg in SBF is relatively dense (Fig. 2b), but there are many large cracks on the surface caused by the internal stress release from dehydration of the dense corrosion product during SEM examination. EDS shows uniform distributions of Mg, O, P, and Ca and the presence of $Mg(OH)_2$, MgO, and Ca-P deposits. The results indicate that Ca and P in the SBF affect the corrosion behavior of pure Mg in SBF and participate in the growth of the corrosion product layer.

The cross-sectional morphology of the corrosion product film after immersion in the NaCl solution and SBF for 168 h is depicted. The former shows primarily localized corrosion, with a maximum corrosion depth of up to 40 μm (Fig. 2c). The localized micro-electrochemical corrosion originates mainly from grain boundary defects or impurities in the pure Mg. EDS reveals mainly Mg and O. In contrast, after immersion in SBF for 168 h, a distinct layered structure emerges, with the upper layer predominantly enriched with Ca-P deposits and the lower layer comprising typical corrosion products of $Mg(OH)_2$ or MgO (Fig. 2d). This layered structure stems from the high corrosion rate of pure Mg in the initial stage of corrosion, leading to the rapid formation of OH^-. The buffering ion, HPO_4^{2-}, in the physiological solution is easily converted to PO_4^{3-} in a high-pH environment to facilitate the rapid formation of low-solubility $Ca_3(PO_4)_2$ which is deposited on the surface. The Ca-P deposited film is denser than $Mg(OH)_2$ or MgO and has blocking effects on

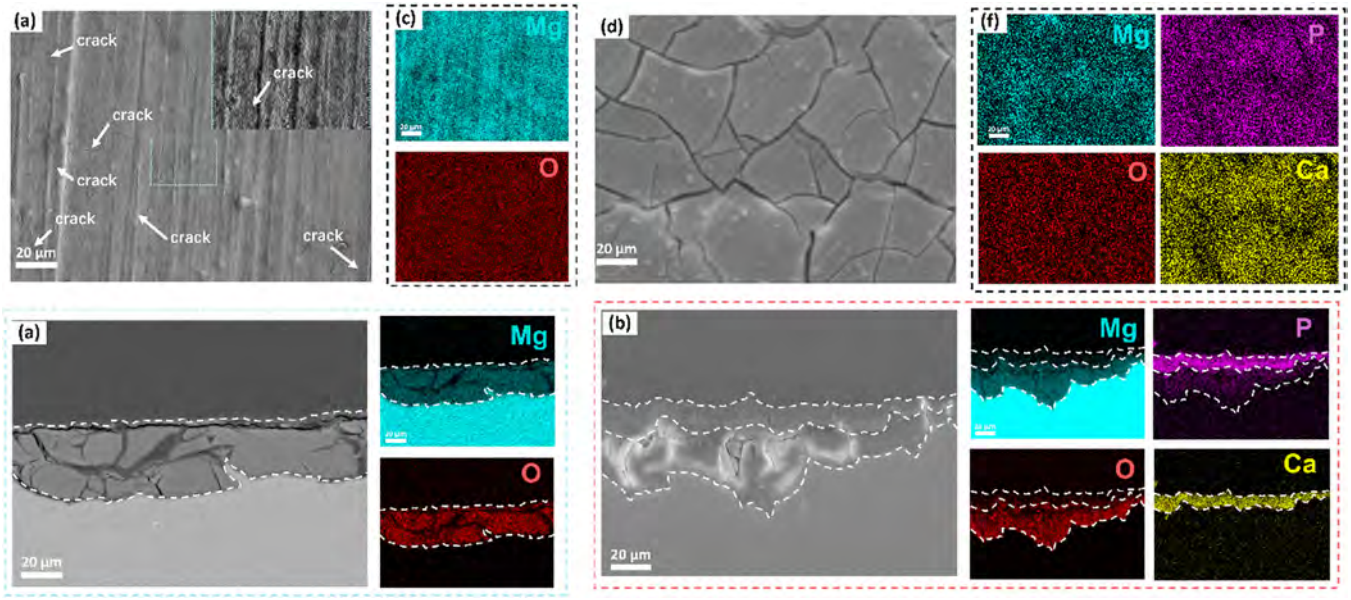

Fig. 2. Surface and Cross-sectional morphology and elemental distributions after immersion of pure Mg for 168 h: (a, c) In the NaCl solution; (b, d) In the SBF.

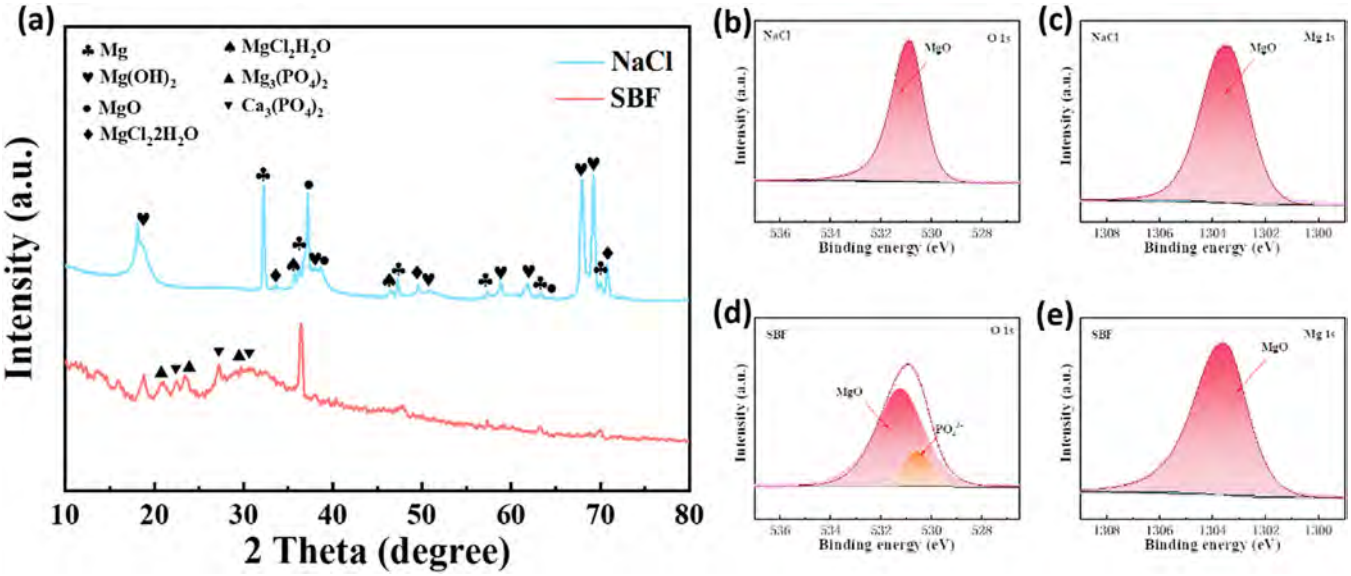

Fig. 3. Chemical composition of the pure Mg: (a) XRD spectra, XPS spectra: (b) O 1*s* in the NaCl solution; (c) Mg 1*s* in the NaCl solution; (d) O 1*s* in SBF and (e) Mg 1*s* in SBF.

the corrosive medium to reduce the corrosion rate in SBF. Additionally, the surface morphology of pure Mg after removing the corrosion products suggests a localized corrosion (Fig. S2).

Fig. 3a shows that the pure Mg after immersion in the NaCl solution displays diffraction peaks of $Mg(OH)_2$, MgO, $MgCl_2{\cdot}H_2O$ and $MgCl_2{\cdot}2H_2O$. They indicate that the porous $Mg(OH)_2$/MgO corrosion product film formed during immersion in the NaCl solution is attacked by Cl^- ions, leading to the formation of soluble $MgCl_2$, which affects the protection ability. In comparison, the pure Mg after immersion in SBF shows diffraction peaks of $Mg(OH)_2$, $Mg_3(PO_4)_2$ and $Ca_3(PO_4)_2$. This is because the dissolved Mg^{2+} and Ca^{2+} ions in the SBF react with $H_2PO_4^-$/HPO_4^{2-} to form insoluble phosphates that cover the substrate. Therefore, the corrosion products on the pure Mg in SBF are more compact. It is worth noting that there is also a typical "bread loaf" peak between 10° and 35°, indicating the amorphous phases in the corrosion products. Amorphous phases are typically related to the rapid deposition of corrosion products, resulting in atoms not being arranged in a regular manner [62].

Fig. 3b displays the O 1*s* peak on pure Mg after immersion in the NaCl solution with only one peak at 530.85 eV for MgO. XRD and EDS further disclose that the corrosion

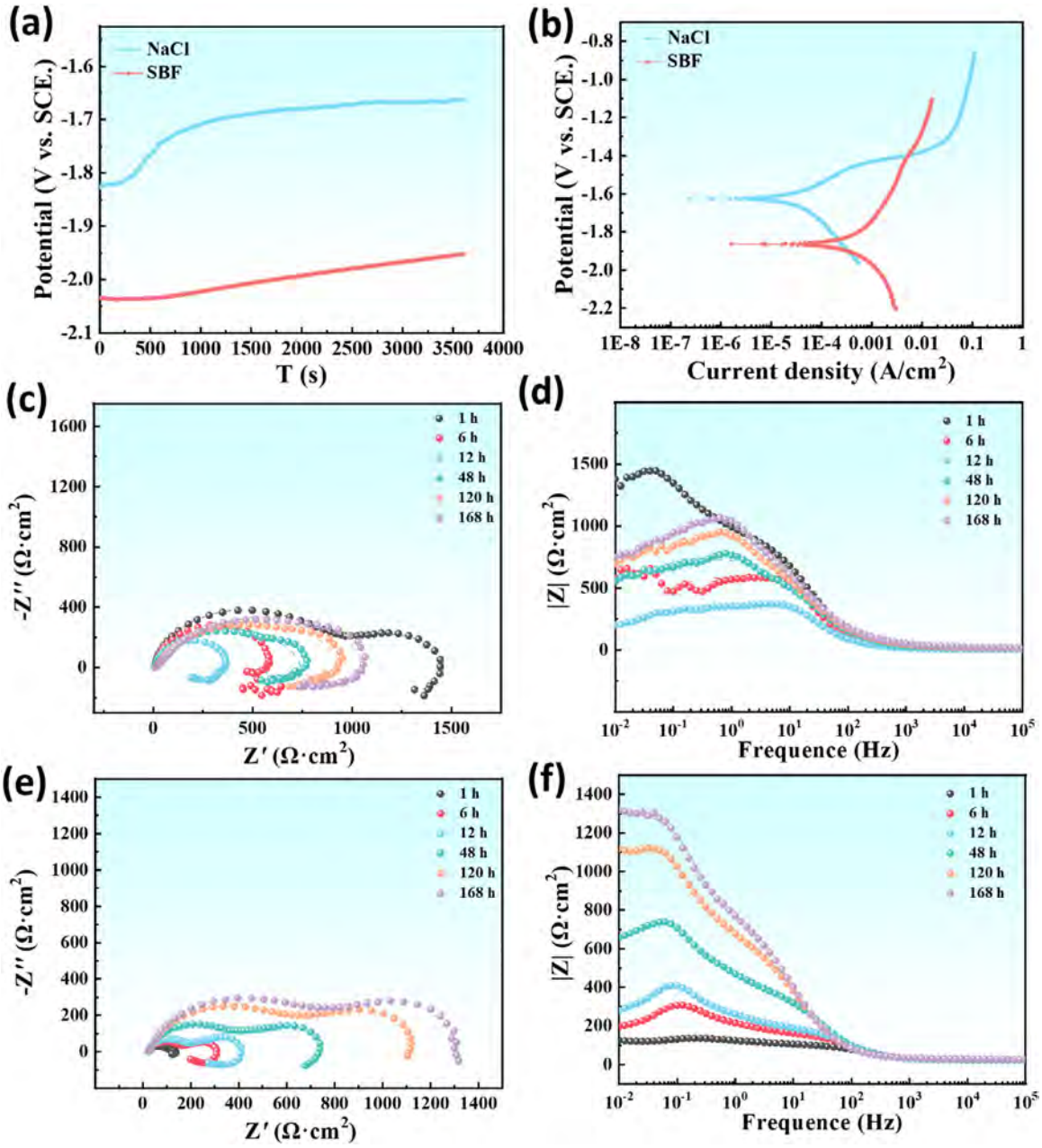

Fig. 4. (a) OCP and (b) Tafel plots of the pure Mg immersed in the NaCl solution and SBF after 1 h, EIS results of pure Mg in the NaCl solution: (c) Nyquist plots and (d) Bode impedance plots, EIS results of pure Mg in SBF: (e) Nyquist plots and (f) Bode impedance plots.

product comprises MgO and $Mg(OH)_2$. In comparison, the pure Mg after immersion in SBF shows not only the MgO peak at 531.21 eV (Fig. 3d), but also a phosphate peak at 530.55 eV. The Ca 2*p* and P 2*p* peaks in Fig. S3 also indicate the formation of calcium phosphate. XRD and EDS reveal that the corrosion product layer contains MgO, $Mg(OH)_2$, $Ca_3(PO_4)_2$, $Mg_3(PO_4)_2$, and their amorphous counterparts. The binding energy of MgO in the Mg 1s spectrum increases slightly in SBF compared to the NaCl solution, possibly due to the different proportions of Mg-containing corrosion products (Fig. 3c and e).

Fig. 4 shows the electrochemical performance of pure magnesium in the NaCl and SBF. The OCP and Tafel curves of the pure Mg are determined after immersing for 1 h (Fig. 4a, b). As the immersion time increases, the OCP values of pure Mg in the NaCl solution rise from −1.83 V to −1.74 V within 10 min, followed by a slow increase and stabilization at −1.66 V. In contrast, the OCP values of pure Mg in SBF gradually increase from −2.03 V to −1.95 V. This suggesting a faster corrosion rate of pure Mg in the early stage in SBF due to $HPO_4^{2-}/H_2PO_4^-$, but the corrosion product film formed in SBF showing a continuing enhanced protection ca-

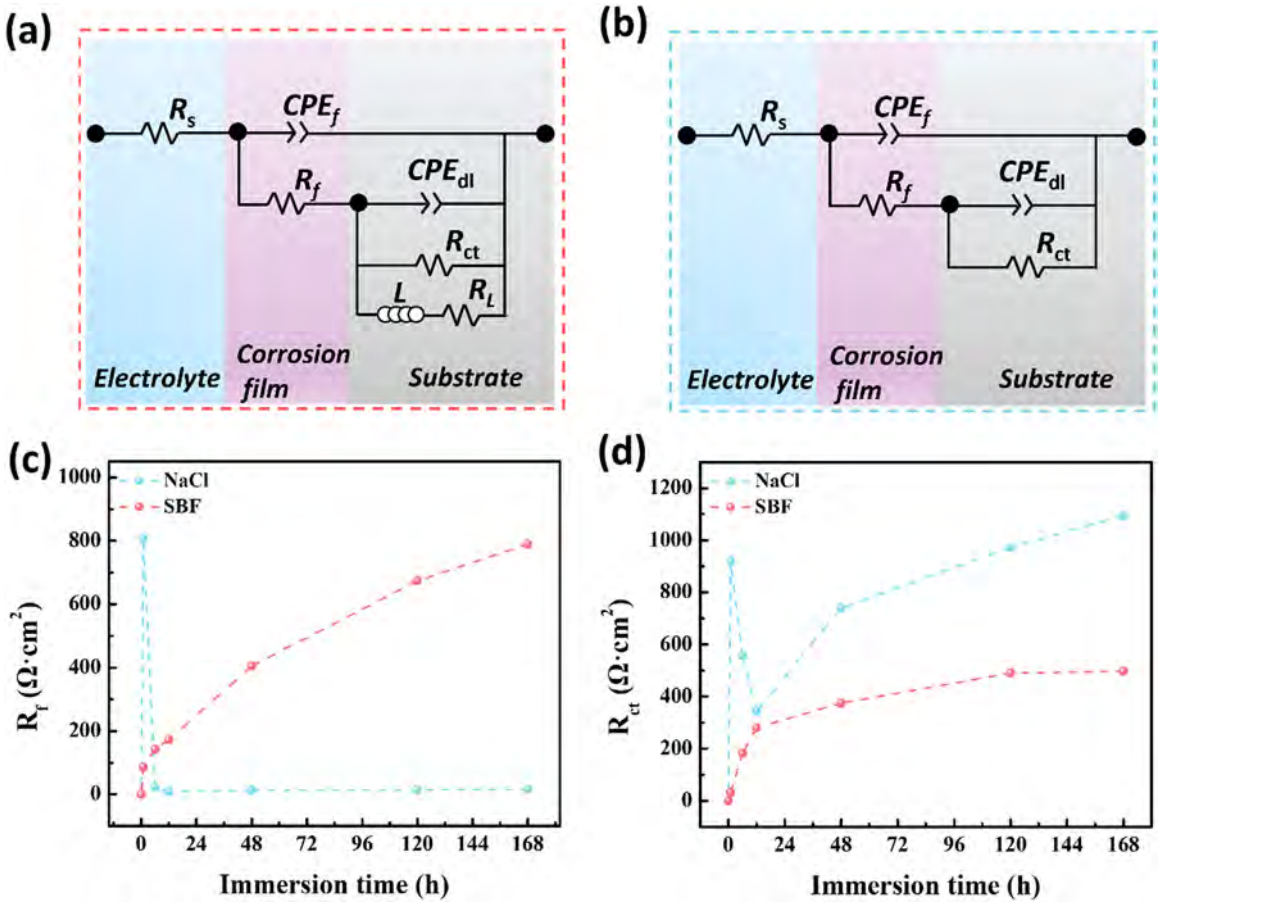

Fig. 5. EIS data fitting and ECs: (a) R(Q(R(QR(LR)))) and (b) R(Q(R(QR))), Changes of the electrical components after EIS data fitting: (c) R_f and (d) R_{ct}.

Table 1
Corrosion potentials and corrosion current densities of pure Mg in the NaCl solution and SBF.

Solutions	Corrosion potentials (V)	Corrosion current densities (A·cm^{-2})
NaCl solution	−1.63	4.00×10^{-5}
SBF	−1.86	2.79×10^{-4}

pability. Fig. 4b and Table 1 present the corrosion potential of −1.63 V and corrosion current density of 4.00×10^{-5} A·cm^{-2} for pure Mg in the NaCl solution, whereas the corrosion potential is −1.86 V and corrosion current density is 2.79×10^{-4} A·cm^{-2} for pure Mg in SBF. Additionally, the varying degree of passivation observed from the anodic region of the Tafel curves for both the NaCl solution and SBF further confirms the difference in the corrosion resistance.

Fig. 4c to f show the EIS results of pure Mg immersed in the NaCl solution and SBF for 168 h. The Nyquist plots of pure Mg immersed in the NaCl solution show that the capacitance loop radius reaches the peak value after 1 h, decreases rapidly, and then increases gradually after 12 h (Fig. 4c). The low-frequency impedance plots exhibit a similar variation, rapid increase to a maximum of 1376.52 Ω·cm^2 after 1 h, decrease to 200.16 Ω·cm^2 after 12 h, and gradual increase to 747.53 Ω·cm^2 afterward (Fig. 4d). Moreover, a significant inductive behavior is observed in the low-frequency region, indicating continuous localized corrosion. This indicates that the initial corrosion product film $Mg(OH)_2$ has a protective effect, but is unstable and susceptible to attack by Cl^-, leading to its transformation into water-soluble $MgCl_2$. Fig. 4e depicts the Nyquist plots of pure Mg immersed in SBF for 168 h. The radius of the capacitance loop increases gradually and inductive behavior in the low-frequency region disappears after 120 h, indicating that the corrosion product provides sustained protective effects due to the denser Ca-P deposit in SBF. The changes in the low-frequency impedance values in Fig. 4f confirm this observation, as manifested by the increase from 126.53 Ω·cm^2 after 1 h to 1318.76 Ω·cm^2 after 168 h.

Based on the Bode phase angles in Fig. S4, fitting of the EIS results is conducted to determine the specific equivalent circuits (EC) of R(Q(R(QR(LR)))) and R(Q(R(QR))), as shown in Fig. 5a and b. The capacitive loop in the mid-to-high frequency range is associated with the degradation product films, while the electrochemical behavior in the low-frequency range is attributed to the interfacial reaction of the substrate in the solution. Owing to the non-uniformity caused by the rough, porous, and uneven chemical composition of

Table 2
EC constant phase element coefficients and resistances of pure Mg in the NaCl solution and SBF after fitting.

Immersion time		R_s (Ω·cm^2)	CPE_f (Ω^{-1}·cm^{-2}·s^n)	n_f	R_f (Ω·cm^2)	CPE_{dl} (Ω^{-1}·cm^{-2}·s^n)	n_{dl}	R_{ct} (Ω·cm^2)	L (H·cm^2)	R_L (Ω·cm^2)	χ^2
NaCl solution	1h	6.848	1.62×10^{-5}	0.9248	805.9	1.23×10^{-3}	0.5381	920	11,000	584.2	3.80×10^{-4}
	6h	7.229	9.19×10^{-6}	0.9703	21.58	8.56×10^{-6}	0.9468	555.9	2083	639.9	1.54×10^{-3}
	12h	6.23	9.52×10^{-6}	0.9775	9.662	1.30×10^{-5}	0.9529	343.9	2129	341.9	3.06×10^{-3}
	48h	7.181	4.31×10^{-5}	0.7505	13.03	1.32×10^{-6}	0.9773	739.5	7264	2059	2.14×10^{-3}
	120h	8.689	4.03×10^{-5}	0.6473	13.96	2.03×10^{-1}	0.7602	973.6	5797	3030	1.09×10^{-3}
	168h	10.31	1.43×10^{-5}	0.6968	16.5	4.49×10^{-5}	0.6989	1094	5979	2277	1.17×10^{-3}
SBF	1h	22.88	5.14×10^{-5}	0.8132	86	6.77×10^{-4}	0.7814	31.29	83.9	6.588	5.26×10^{-4}
	6h	23.56	3.87×10^{-5}	0.8467	142	3.47×10^{-3}	0.6734	182.3	558.4	30.36	5.35×10^{-4}
	12h	22.8	3.65×10^{-5}	0.8582	172.9	2.85×10^{-3}	0.6585	280.7	1265	83.11	6.56×10^{-4}
	48h	24.19	5.68×10^{-5}	0.8096	405	2.22×10^{-3}	0.7652	374.5	4247	298.7	9.21×10^{-4}
	120h	27.79	6.78×10^{-5}	0.8187	673.8	2.08×10^{-3}	0.8443	489.9	1.15×10^4	933.3	1.57×10^{-3}
	168h	28.82	6.44×10^{-5}	0.83	789.8	1.70×10^{-3}	0.9539	497.1	—	—	1.79×10^{-3}

the degradation product film, the ideal capacitors and resistors cannot be used to analyze the interfacial charge transfer processes. Therefore, a constant phase element (CPE) expressed by Eq. (3) is chosen to describe the non-ideal resistance and capacitance of the coating:

$$Z_{CPE} = \frac{1}{T(j\omega)^n} \quad -1 \le n \le 1 \quad , \tag{3}$$

where Z_{CPE} represents the resistance of the CPE, T is the CPE coefficient, n is the CPE index, $j = \sqrt{-1}$ is the imaginary unit, and ω is the angular frequency (related to the frequency f, ω=2πf). When n is equal to −1, 0, and 1, it is simulated as an ideal inductor, ideal resistor, and ideal capacitor, respectively. When local corrosion occurs, an inductor element needs to be added to the EC. In the EC, R_s represents the resistance of the sample in the solution. CPE_f and R_f represent the capacitance and resistance of the corrosive product film on the sample, which represents the protective effect of the corrosive product film. CPE_{dl} and R_{ct} are the double-layer capacitance at the substrate interface and charge transfer resistance during the Faraday process, respectively, representing the degree of degradation of the sample.

Table 2 shows the electrical components obtained by fitting the EIS data of the pure Mg in the NaCl solution and SBF, and the changes in the R_f and R_{ct} are shown in Fig. 5c and d. Typically, the larger the value of R_f, the stronger the protective effect of the corrosive product film. A larger R_{ct} translates into slower corrosion [63]. The R_f of pure Mg in the NaCl solution decreases initially and then increases, while R_f in the SBF increases gradually (Fig. 5c). In the initial 1 h, R_f of the pure Mg in the NaCl solution is larger than that in the SBF, showing values of 805.8 Ω·cm^2 and 86 Ω·cm^2, respectively. This indicates that the corrosion product film in the NaCl solution provides better protection to the substrate in the early stage. However, after 168 h, the R_f values of the pure Mg in the NaCl solution and SBF reverse compared to those in the first 1 h, showing values of 16.5 Ω·cm^2 and 789.8 Ω·cm^2, respectively. This reversal arises from the structure and composition of the corrosion product film. It is evident that thicker Ca-P deposit resists long-term corrosion attacks by anions. The R_{ct} value in Fig. 5d shows the same variation as R_f. The formation of the corrosion product film effectively limits the mass transfer of the corrosion reaction at the substrate interface, thereby reducing the corrosion rate.

To investigate the significant differences in the corrosion rates and R_f of pure Mg during initial immersion (1 h) in SBF and the NaCl solution, the cross-sectional morphology and microstructure are analyzed, as shown in Fig. 6. After 1 h in the NaCl solution, a uniform corrosion product film with a thickness of ~1 μm is formed on the pure Mg. The film exhibits minimal cracking and no localized corrosion (Fig. 6a). EDS indicates the presence of primarily Mg and O, suggesting the dominance of $Mg(OH)_2$ and MgO. In contrast, after 1 h in SBF, the corrosion product film on pure Mg is thicker and around 8 μm. It has a stratified structure similar to that observed after 168 h (Fig. 6b). EDS reveals an upper layer ~3 μm thick composed of Ca and P, while the lower

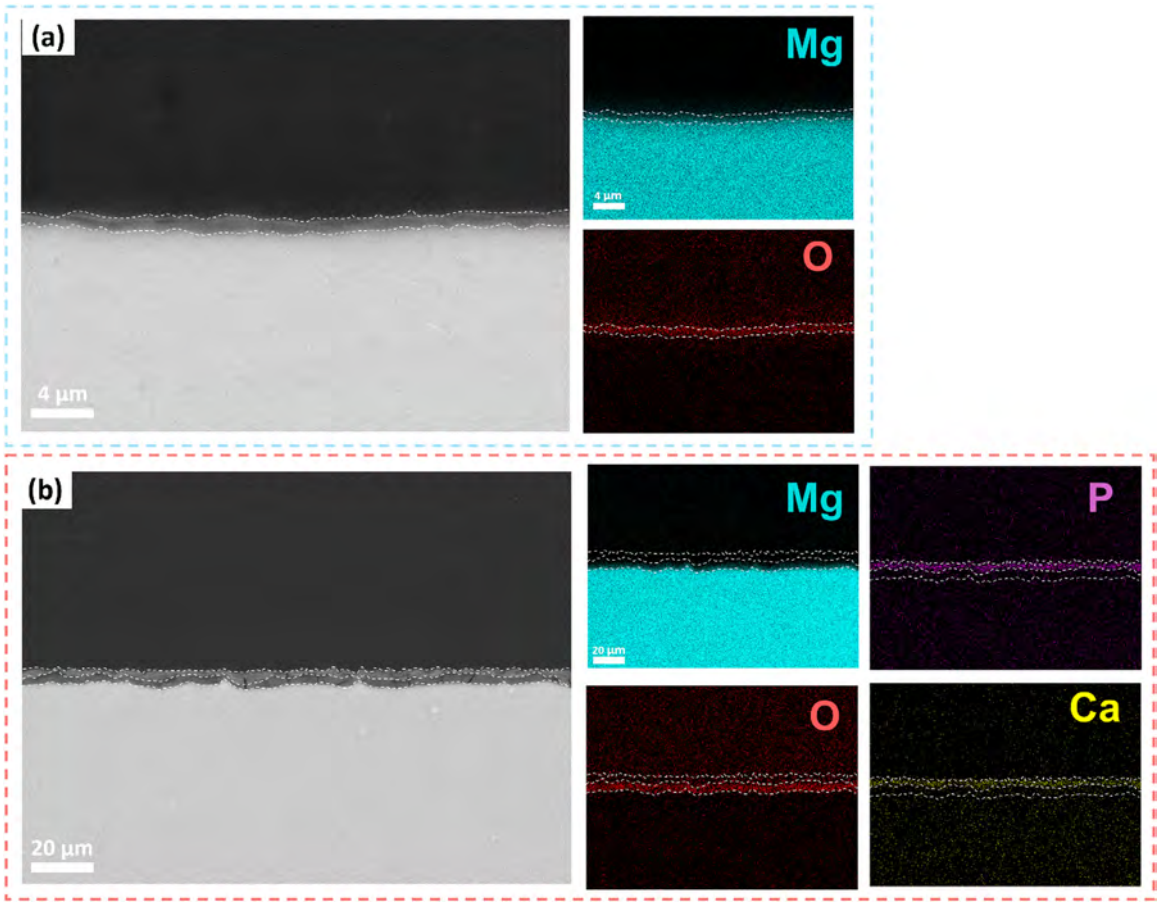

Fig. 6. Cross-sectional morphology and elemental distributions of pure Mg after 1 h: (a) NaCl solution and (b) SBF.

layer ~5 μm thick consists of Mg and O with cracks. This phenomenon can be ascribed to faster hydrogen evolution in SBF affecting the compactness of the corrosion product film. Therefore, the thicker corrosion product film in SBF does not have a larger R_f.

Furthermore, the deposition of surface corrosion products of pure Mg in the NaCl solution and SBF at an earlier time (5 min) are investigated. A thin corrosion product film is grown *in situ* on the pure Mg after immersion in the NaCl solution for 1 min, and it does not cover the scratches formed by polishing (Fig. 7a). The enlarged surface reveals that the main morphology is a typical nano-sheet structure of $Mg(OH)_2$, and EDS indicates the generation of $Mg(OH)_2$/MgO corrosion products. After immersion for 2 and 5 min, the nano-sheet structure on the surface remains largely unchanged, with only slight increases in size (Fig. 7b and c). In contrast, a relatively thick and dense corrosion product film covers the surface of pure Mg after immersion for 1 min in SBF, but some cracks are present (Fig. 7d). EDS shows that Mg, P, O, and Ca are evenly distributed on the pure Mg and the formation of Ca-P deposits. This is because pure Mg undergoes rapid corrosion in SBF, leading to the generation of local alkaline conditions that promote the formation of low-solubility $Ca_3(PO_4)_2$ and causing the pure Mg to be quickly covered by Ca-P deposits. The cracks are caused by the dehydration-induced stress release of $Mg(OH)_2$ corrosion products. As the immersion for 2 and 5 min, the coverage of corrosion products gradually increases, with almost no change in the elements present, but the number and size of cracks increase (Fig. 7e, f). This is because more $Mg(OH)_2$ is formed during deposition, and dehydration-induced stress is more pronounced during SEM, causing cracks to expand when the stress reaches the relatively dense Ca-P deposit layer on the surface, resulting in the appearance of larger cracks after 168 h. These results indicate that the deposition of corrosion products on pure Mg in SBF is faster and thicker in the early stage, but the faster hydrogen evolution rate leads to a looser $Mg(OH)_2$ structure in the corrosion product film. Fortunately, the corrosion rate of the substrate continues to decrease due to the protection of the outer Ca-P deposit layer.

To study the corrosion and degradation of pure Mg in the physiological environment, we implant the materials into the medullary cavity of mouse femurs for *in vivo* assessment. Beforehand a biocompatibility evaluation is conducted on the pure Mg, and the results of the cell experiments show that the pure Mg is biocompatible and does not exhibit cytotoxicity. The HUVEC cells exhibit normal proliferation, differentiation, and growth (Figs. S5, S6). Subsequently, 0.6 mm diameter pure Mg rods are implanted into mice and retrieved for degradation analysis after 4 weeks, as shown in Fig. 8a.

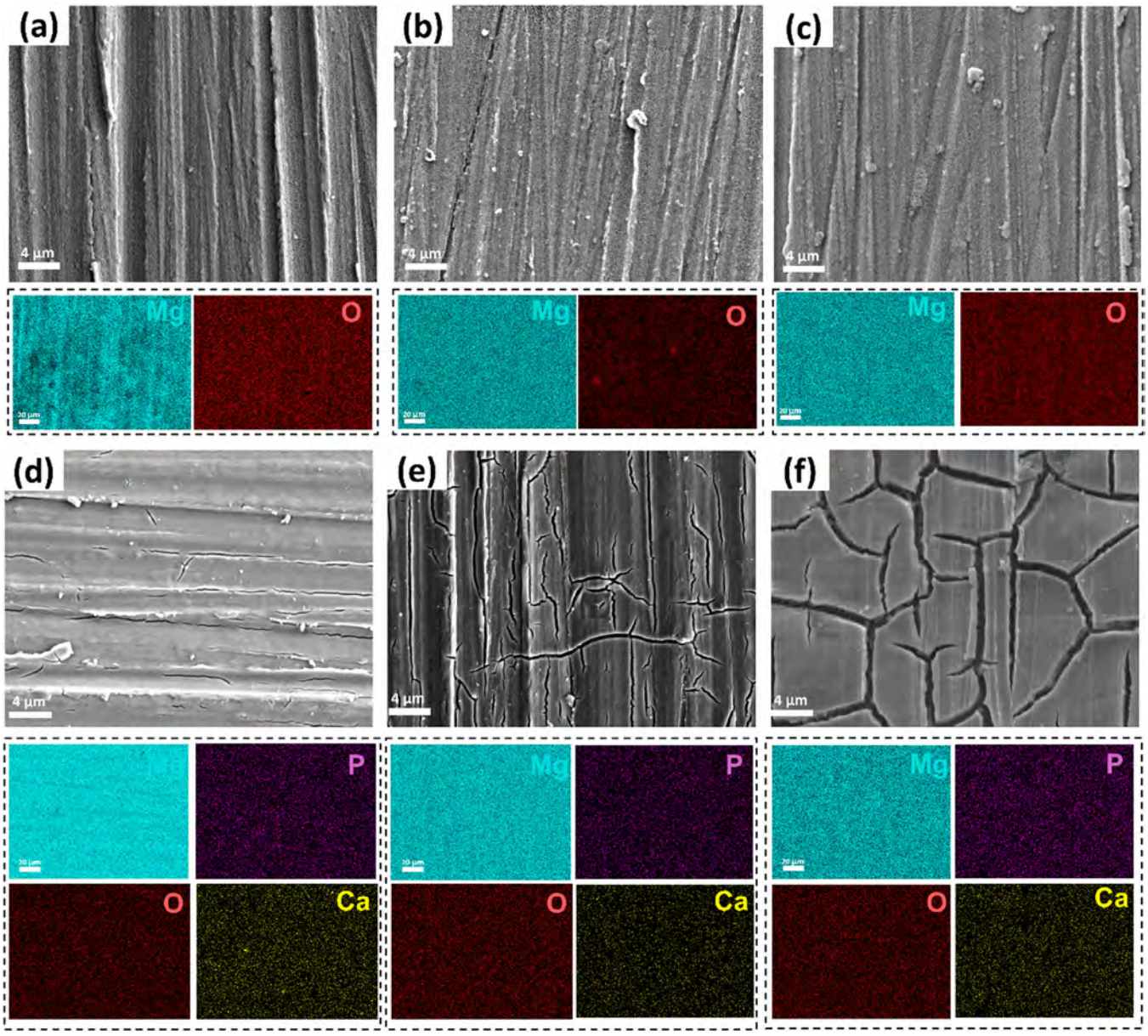

Fig. 7. Surface morphology and elemental distributions of pure Mg in the early stage of corrosion in the NaCl solution: (a) 1 min; (b) 2 min; (c) 5 min, and in SBF: (d) 1 min; (e) 2 min; (f) 5 min.

The cross-sectional morphology and elemental composition of the pure Mg rods are presented in Fig. 8b and c. After 4 weeks in the mouse femur, the pure Mg is corroded, leaving irregular remnants indicating severe localized corrosion *in vivo*. EDS indicates the presence of a 20–40 μm corrosion product film on the surface with a layered structure similar to that observed in the immersion corrosion in SBF *in vitro*. The outer layer primarily comprises Mg, P, O, and Ca, while the inner layer consists solely of Mg and O, indicating the formation of the Ca-P sediment. The other degradation patterns are nearly identical to those observed from the SBF soaking test. This suggests that the degradation of pure Mg in the physiological environment is localized corrosion, with the formation of a Ca-P deposit corrosion product film on the surface providing protection to the substrate. However, it cannot resist long-term corrosion degradation, and the corrosion products will gradually be consumed and degrade in the physiological environment, ultimately resulting in complete degradation *in vivo*.

Fig. 9 illustrates the degradation mechanisms of pure Mg in the NaCl solution and SBF. As shown in Fig. 9a, corrosion of pure Mg in the NaCl solution typically manifests as localized corrosion arising from micro galvanic corrosion caused by defects at grain boundaries and impurities at these boundaries. Initially, corrosion of pure Mg is relatively uniform, releasing Mg^{2+} and OH^- ions and rapidly forming $Mg(OH)_2$ deposits, as indicated by Eq. (4).

$$Mg^{2+} + 2OH^- \rightarrow Mg(OH)_2 \quad (4)$$

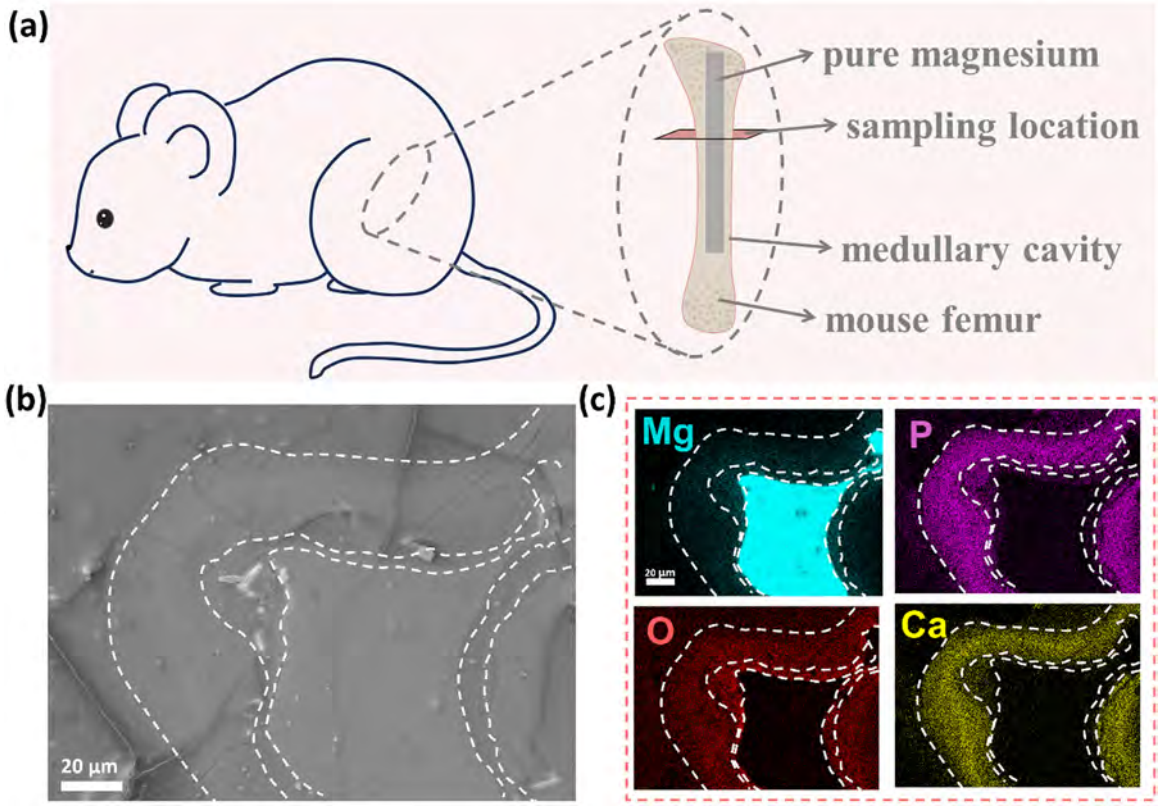

Fig. 8. Degradation pure Mg in mice *in vivo*: (a) Schematic diagram of pure Mg implantation in mice; (b) Cross-sectional morphology; (c) Elemental analysis.

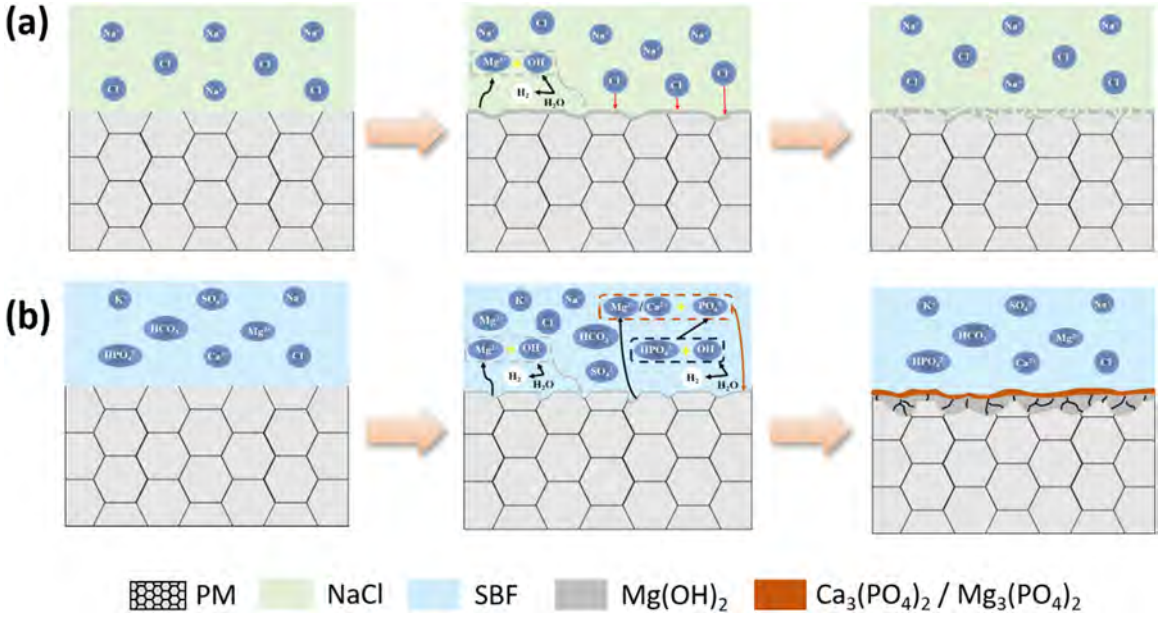

Fig. 9. Degradation mechanism of pure Mg: (a) NaCl solution and (b) SBF.

Although the $Mg(OH)_2$ deposit can provide protection to the substrate, with increasing immersion time and elevated pH of the solution, $Mg(OH)_2$ is easily attacked by Cl^- in the solution and transformed into soluble $MgCl_2$, as shown by Eq. (5). This leads to the destruction of the corrosion product film and localized corrosion at defect positions, thus resulting in a more porous corrosion product film and reduced protective effect.

$$Mg(OH)_2 + 2Cl^- \rightarrow Mg^{2+} + 2OH^- \quad (5)$$

Fig. 9b illustrates the degradation mechanism of pure Mg in SBF. In the early stage of degradation in the physiological

environment, hydrogen in the medium accelerates the corrosion reaction with the a-Mg phase in pure Mg, resulting in the release of Mg^{2+} and OH^-. The localized alkaline environment further causes the transformation of HPO_4^{2-} into PO_4^{3-} in the medium. PO_4^{3-} readily reacts with Ca^{2+} and Mg^{2+} in the medium to form low-solubility precipitates of $Ca_3(PO_4)_2$ and $Mg_3(PO_4)_2$, which preferentially deposit on the surface, as shown by Eqs. (6)–(8).

$$HPO_4^{2-} + OH^- \rightarrow PO_4^{3-} + H_2O \quad (6)$$

$$3Ca^{2+} + 2PO_4^{3-} \rightarrow Ca_3(PO_4)_2 \quad (7)$$

$$3Mg^{2+} + 2PO_4^{3-} \rightarrow Mg_3(PO_4)_2 \quad (8)$$

The phosphate layer formed on the surface is more compact in structure compared to the traditional corrosion product $Mg(OH)_2$. Therefore, early deposition of the phosphate layer provides certain protection for pure Mg. Furthermore, a large amount of Mg^{2+} and OH^- generated at the localized corrosion sites will rapidly form $Mg(OH)_2$ deposits. As the corrosion continues, the film plays a protective role, leading to the transition to the next corrosion stage. In this stage, due to the relatively fast corrosion rate of pure Mg, diffusion of HPO_4^{2-} and Ca^{2+} from the medium toward the substrate interface is slower than the corrosion rate at the interface. As a result, a uniform and dense Ca-P, Mg-P layer cannot be formed inside the corrosion product film, and mostly localized $Mg(OH)_2$ deposits are observed. Eventually, the corrosion product film forms a layered structure, where the thicker phosphate layer on the surface effectively inhibits the attack of Cl^- leading to a gradual decrease in the corrosion rate.

4. Conclusion

The degradation behavior of pure Mg in the physiological environment is investigated by immersion and hydrogen evolution experiments. Compared to the NaCl solution (0.60 $mm{\cdot}y^{-1}$), the corrosion rate of pure Mg in SBF is faster, reaching 2.81 $mm{\cdot}y^{-1}$, due to $HPO_4^{2-}/H_2PO_4^-$. The hydrogen evolution rate rapidly decreases within the first 12 h and then stabilizes in SBF. The corrosion product film on the pure Mg display a layered structure, with the upper layer being dense $Ca_3(PO_4)_2/Mg_3(PO_4)_2$ and the lower layer being porous $Mg(OH)_2$/MgO. EIS shows that the capacitive arc radius and impedance of pure Mg in SBF gradually increases, indicating that the corrosion resistance increases gradually during degradation. The low-solubility product of $Ca_3(PO_4)_2$ is deposited in SBF to protect the substrate, thus blocking the dissolution of the porous corrosion product $Mg(OH)_2$ by Cl^- and significantly improving the corrosion resistance of the substrate. The pure Mg implanted in the medullary cavity of the mouse femur for 4 weeks shows that the pure Mg also produces a layered structure containing enriched $Ca_3(PO_4)_2$ in the outer layer, which is consistent with that observed in the physiological environment *in vitro*.

Declaration of competing interest

Tao Ying, Xiaoqin Zeng is an editorial board member/editor-in-chief for Journal of Magnesium and Alloys and was not involved in the editorial review or the decision to publish this article. All authors declare that there are no competing interests.

CRediT authorship contribution statement

Chenyu Wang: Writing – original draft, Supervision, Investigation, Formal analysis, Data curation, Conceptualization. **Mingshan Sun:** Investigation, Formal analysis, Data curation. **Chao Yang:** Writing – review & editing, Project administration, Investigation, Funding acquisition, Conceptualization. **Haiyang Wang:** Investigation, Data curation. **Jie Wang:** Software, Investigation, Data curation. **Lin Mao:** Visualization, Supervision, Methodology. **Yao Yang:** Investigation, Formal analysis, Data curation, Conceptualization. **Tao Ying:** Resources, Methodology, Conceptualization. **Paul K. Chu:** Writing – review & editing, Resources, Funding acquisition. **Xiaoqin Zeng:** Writing – review & editing, Investigation, Funding acquisition, Conceptualization.

Acknowledgments

This work was supported by the National Natural Science Foundation of China (52127801), Postdoctoral Fellowship Program of CPSF under Grant Number GZC20231545, China Postdoctoral Science Foundation (2024T170557 and 2023M742224), Shanghai Post-doctoral Excellence Program (No. 2023440), and City University of Hong Kong Donation Grants (DON-RMG No. 9229021 and 9220061).

Supplementary materials

Supplementary material associated with this article can be found, in the online version, at doi:10.1016/j.jma.2024.05.012.

References

[1] V. Tsakiris, C. Tardei, F.M. Clicinschi, J. Magnes. Alloys 9 (2021) 1884–1905.
[2] J. Niu, H. Huang, J. Pei, Z.X. Jin, S. Guan, G. Yuan, Biomater. Transl. 2 (2021) 236–247.
[3] M. Echeverry-Rendon, J.P. Allain, S.M. Robledo, F. Echeverria, M.C. Harmsen, Mater. Sci. Eng. C 102 (2019) 150–163.
[4] M. Daroonparvar, M.U. Khan, Y. Saadeh, C.M. Kay, R.K. Gupta, A.K. Kasar, P. Kumar, M. Misra, P.L. Menezes, H.R. Bakhsheshi-Rad, Mater. Chem. Phys. 256 (2020) 123627.
[5] X. Gao, C.Y. Dai, Q. Jia, C. Zhai, H. Shi, Y. Yang, B.C. Zhao, H. Cai, E.S. Lee, H.B. Jiang, Scanning 2021 (2021) 5530788.
[6] Y.F. Zheng, Y.F. Wu, Acta Metall. Sin. 53 (2017) 257–297.
[7] J. Nagels, M. Stokdijk, P.M. Rozing, J. Shoulder Elb. Surg. 12 (2003) 35–39.
[8] S. Agarwal, J. Curtin, B. Duffy, S. Jaiswal, Mater. Sci. Eng. C 68 (2016) 948–963.
[9] Y.C. Su, J.Y. Fu, J.C. Zhou, E. Georgas, S. Du, Y.X. Qin, Y.D. Wang, Y.F. Zheng, D.H. Zhu, Bioact. Mater. 20 (2023) 243–258.

[10] G.Y. Yuan, J.L. Niu, Acta Metall. Sin. 53 (2017) 1168–1180.
[11] Y.F. Zheng, X.N. Gu, F. Witte, Mater. Sci. Eng. R Rep. 77 (2014) 1–34.
[12] Y. Su, J. Lin, Y. Su, W. Zai, G. Li, C. Wen, Scanning (2018) 6519310 2018.
[13] G. Song, T.T. Li, L. Chen, Mater. Sci. Eng. A 736 (2018) 306–315.
[14] G. Li, L. Zhang, L. Wang, G. Yuan, K. Dai, J. Pei, Y. Hao, Acta Biomater. 65 (2018) 486–500.
[15] Y. Zhang, J. Xu, Y.C. Ruan, M.K. Yu, M. O'Laughlin, H. Wise, D. Chen, L. Tian, D. Shi, J. Wang, S. Chen, J.Q. Feng, D.H. Chow, X. Xie, L. Zheng, L. Huang, S. Huang, K. Leung, N. Lu, L. Zhao, L. Qin, Nat. Med. 22 (2016) 1160–1169.
[16] N. Oshibe, E. Marukawa, T. Yoda, H. Harada, J. Biomater. Appl. 33 (2019) 1157–1167.
[17] Y.C. Hsu, Y.P. Lu, S.Y. Wang, Y.F. Zheng, D.D. Xia, Y.S. Liu, J. Magnes. Alloys 11 (2023) 3399–3426.
[18] V.V. Troitskii, D.N. Tsitrin, Khirurgiia (Mosk) 8 (1944) 41–44.
[19] F. Witte, V. Kaese, H. Haferkamp, E. Switzer, A. Meyer-Lindenberg, C.J. Wirth, H. Windhagen, Biomaterials 26 (2005) 3557–3563.
[20] J.M. Seitz, A. Lucas, M. Kirschner, JOM 68 (2016) 1177–1182.
[21] J.W. Lee, H.S. Han, K.J. Han, J. Park, H. Jeon, M.R. Ok, H.K. Seok, J.P. Ahn, K.E. Lee, D.H. Lee, S.J. Yang, S.Y. Cho, P.R. Cha, H. Kwon, T.H. Nam, J.H. Han, H.J. Rho, K.S. Lee, Y.C. Kim. Mantovani, Proc. Natl. Acad. Sci. U. S. A. 113 (2016) 716–721.
[22] J. Kuhlmann, I. Bartsch, E. Willbold, S. Schuchardt, O. Holz, N. Hort, D. Höche, W.R. Heineman, F. Witte, Acta Biomater. 9 (2013) 8714–8721.
[23] D.L. Zhao, T.T. Wang, J.L. Kuhlmann, Z.Y. Dong, S.N. Chen, M. Joshi, P. Salunke, V.N. Shanov, D. Hong, P.N. Kumta, W.R. Heineman, Acta Biomater. 36 (2016) 361–368.
[24] R. Wlodarczyk, M. Sierka, K. Kwapien, J. Sauer, E. Carrasco, A. Aumer, J.F. Gomes, M. Sterrer, H. Freund, J. Phys. Chem. C 115 (2011) 6764–6774.
[25] M. Ončák, R. Włodarczyk, J. Sauer, J. Phys. Chem. Lett. 6 (2015) 2310–2314.
[26] M. Ončák, R. Włodarczyk, J. Sauer, J. Phys. Chem. C 120 (2016) 24762–24769.
[27] Y.Y. Chen, T. Ying, Y. Yang, J.Y. Wang, X.Q. Zeng, Corros. Sci. 216 (2023) 111106.
[28] T. Takenaka, T. Ono, Y. Narazaki, Y. Naka, M. Kawakami, Electrochim. Acta 53 (2007) 117–121.
[29] P.Y. Zhao, T. Xie, X.M. Xu, H. Zhu, F.Y. Cao, T. Ying, X.Q. Zeng, Metall. Mater. Trans. A 51 (2020) 2509–2522.
[30] Q.C. Zhu, Y.X. Li, F.Y. Cao, D. Qiu, Y. Yang, J.Y. Wang, H. Zhang, T. Ying, W.J. Ding, X.Q. Zeng, Nat. Commun. 13 (2022) 5838.
[31] S.V. Verstraeten, L. Aimo, P.I. Oteiza, Arch. Toxicol. 82 (2008) 789–802.
[32] Y. Nakamura, Y. Tsumura, Y. Tonogai, T. Shibata, Y.N. Ito, Fundam. Appl. Toxicol. Off. J. Soc. Toxicol. 37 (1997) 106–116.
[33] C. Yang, H. Cai, S.H. Cui, J. Huang, J.Y. Zhu, Z.C. Wu, Z.Y. Ma, R.K.Y. Fu, L.Y. Sheng, X.B. Tian, P.K. Chu, Z.Z. Wu, Surf. Coat. Technol. 433 (2022) 128148.
[34] C. Yang, J. Huang, S.H. Cui, R. Fu, L.Y. Sheng, D.K. Xu, X.B. Tian, Y.F. Zheng, P.K. Chu, Z.Z. Wu, J. Magnes. Alloys. (2023), doi:10.1016/j.jma.2023.02.008.
[35] C. Yang, S.H. Cui, R.K.Y. Fu, L.Y. Sheng, M. Wen, D.K. Xu, Y. Zhao, Y.F. Zheng, P.K. Chu, Z.Z. Wu, J. Mater. Sci. Technol. 179 (2024) 224–239.
[36] C. Yang, C.Y. Wang, X.Z. Zhao, Z. Shen, M. Wen, C.C. Zhao, L.Y. Sheng, Y.G. Wang, D.K. Xu, Y.F. Zheng, P.K. Chu, X.Q. Zeng, Mater. Des. 239 (2024) 112769.
[37] C.O. Hoog, N. Birbilis, Y. Estrin, Adv. Eng. Mater. 10 (2008) 579–582.
[38] G. Han, J.Y. Lee, Y.C. Kim, J.H. Park, D.I. Kim, H.S. Han, S.J. Yang, H.K. Seok, Corros. Sci. 63 (2012) 316–322.
[39] Z. Savaedi, H. Mirzadeh, R.M. Aghdam, R. Mahmudi, J. Mater. Res. Technol. 19 (2022) 3100–3109.
[40] Y.B. Ren, J.J. Huang, K. Yang, B.C. Zhang, Z.M. Yao, H. Wang, Acta Metall. Sin. 41 (11) (2005) 1228–1232.
[41] L.G. Bland, K. Gusieva, J.R. Scully, Electrochim. Acta 227 (2017) 136–151.
[42] F.A. Rueggeberg, W.F. Caughman, Oper. Dent. 23 (1998) 179–184.
[43] X.B. Chen, D.R. Nisbet, R.W. Li, P.N. Smith, T.B. Abbott, M.A. Easton, D.H. Zhang, N. Birbilis, Acta Biomater. 10 (2014) 1463–1474.
[44] L.C. Zhao, C.X. Cui, Q.Z. Wang, S.J. Bu, Corros. Sci. 52 (2010) 2228–2234.
[45] M.P. Staiger, A.M. Pietak, J. Huadmai, G. Dias, Biomaterials 27 (2006) 1728–1734.
[46] J.J. Huang, K. Yang, Y.B. Ren, B.C. Zhang, G.N.g Yu, Y. Jiang, Rare Met. Mater. Eng. 37 (2008) 629–632.
[47] B. Miao, Y. Lv, M. Liu, M.Q. Li, L.J. Qu, China Surf. Eng. 26 (2013) 45–50.
[48] A.H.M. Sanchez, B.J.C. Luthringer, F. Feyerabend, R. Willumeit, Acta Biomater. 13 (2015) 16–31.
[49] A. Yamamoto, S. Hiromoto, Mater. Sci. Eng. C 29 (2009) 1559–1568.
[50] R.C. Zeng, X.T. Li, S.Q. Li, F. Zhang, E.H. Han, Sci. Rep. 5 (2015) 13026.
[51] D. Mei, S.V. Lamaka, J. Gonzalez, F. Feyerabend, R. Willumeit-Römer, M.L. Zheludkevich, Corros. Sci. 147 (2019) 81–93.
[52] R.C. Zeng, L. Sun, Y.F. Zheng, H.Z. Cui, E.H. Han, Corros. Sci. 79 (2014) 69–82.
[53] W. Ha, Y.J. Kim, J. Alloys Compd. 422 (2006) 208–213.
[54] S. Jr, J.C. Galvan, A. Pardo, M. Merino, R. Arrabal, Open Corros. J. 3 (2010) 80–91.
[55] Z.H. Wen, C.J. Wu, C.S. Dai, F.X. Yang, J. Alloys Compd. 488 (2009) 392–399.
[56] Z.J. Li, X.N. Gu, S.Q. Lou, Y.F. Zheng, Biomaterials 29 (2008) 1329–1344.
[57] J.M. Seitz, K. Collier, E. Wulf, D. Bormann, F.W. Bach, Adv. Eng. Mater. 13 (2011) B313–B323.
[58] R. Ambat, N. Aung, W. Zhou, J. Appl. Electrochem. 30 (2000) 865–874.
[59] W.F. Ng, K.Y. Chiu, F.T. Cheng, Mater. Sci. Eng. C 30 (2010) 898–903.
[60] S. Johnston, Z.M. Shi, A. Atrens, Corros. Sci. 101 (2015) 182–192.
[61] S.V. Lamaka, J. Gonzalez, D. Mei, F. Feyerabend, R. Willumeit-Römer, M.L. Zheludkevich, Adv. Mater. Interfaces 5 (2018) 1800169.
[62] W.L. Johnson, Prog. Mater. Sci. 30 (1986) 81–134.
[63] A.D. King, N. Birbilis, J.R. Scully, Electrochim. Acta 121 (2014) 394–406.

Supporting Information for

Degradation behavior of pure Mg in the physiological medium and growth mechanism of surface corrosion product films

Chenyu Wang [a], Mingshan Sun [b], Chao Yang [a,*], Haiyang Wang [a], Jie Wang [a], Lin Mao [c], Yao Yang [a], Tao Ying [a], Paul K. Chu [d], Xiaoqin Zeng [a,*]

[a] National Engineering Research Center of Light Alloy Net Forming, School of Materials Science and Engineering, Shanghai Jiao Tong University, Shanghai 200240, China

[b] Kunming Branch of the 705 Research Institute of CSSC, Kunming 650101, China

[c] Shanghai Institute for Minimally Invasive Therapy, School of Medical Instrument and Food Engineering, University of Shanghai for Science and Technology, Shanghai, 200093, China

[d] Department of Physics, Department of Materials Science & Engineering, and Department of Biomedical Engineering, City University of Hong Kong, Tat Chee Avenue, Kowloon, Hong Kong, China

∗ Corresponding authors: chaoyang0315@163.com (C. Yang); xqzeng@sjtu.edu.cn (X. Zeng)

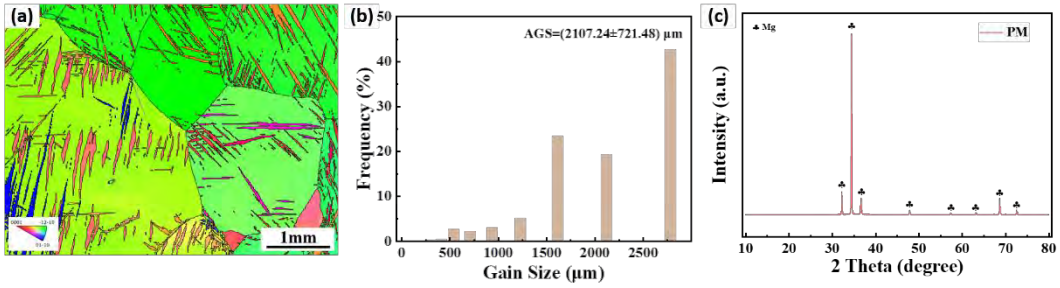

Fig. S1. Characterization of pure Mg: (a) EBSD; (b) Grain size statistics and (c) XRD.

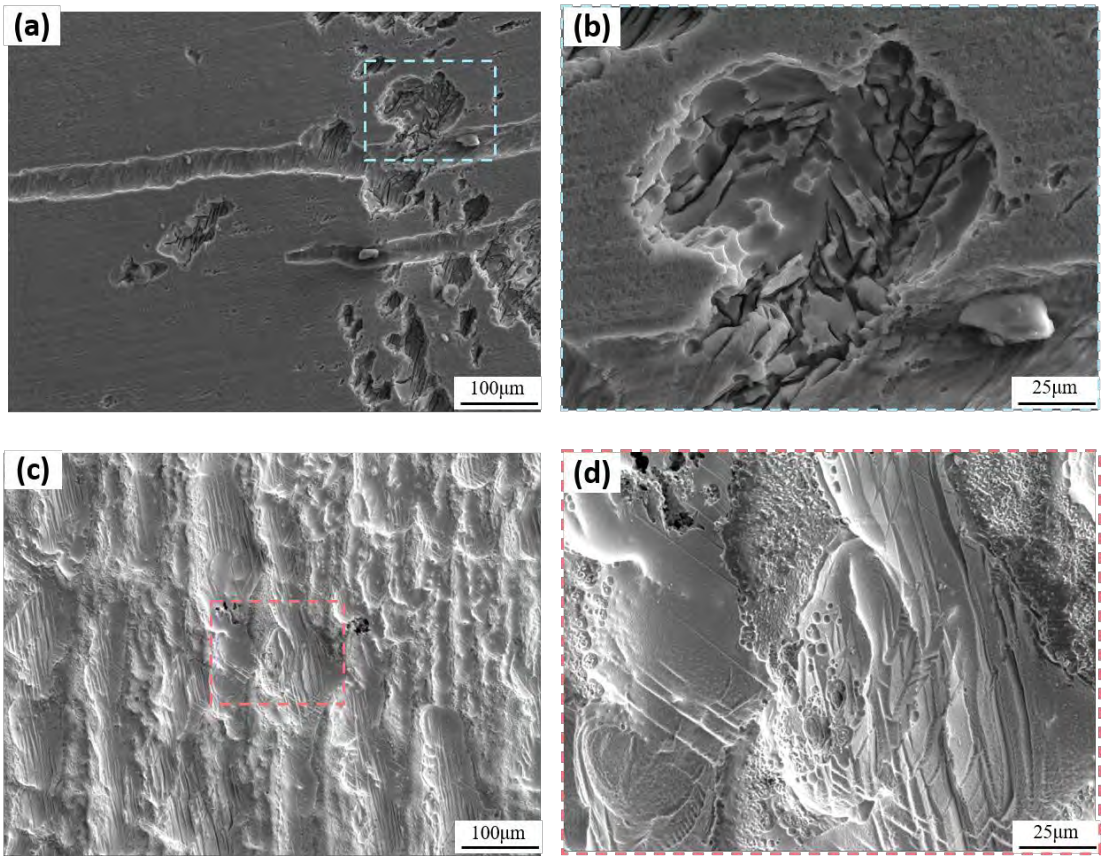

Fig. S2. Surface morphology of pure Mg after corrosion and removal of corrosion products: (a) NaCl solution and (b) SBF

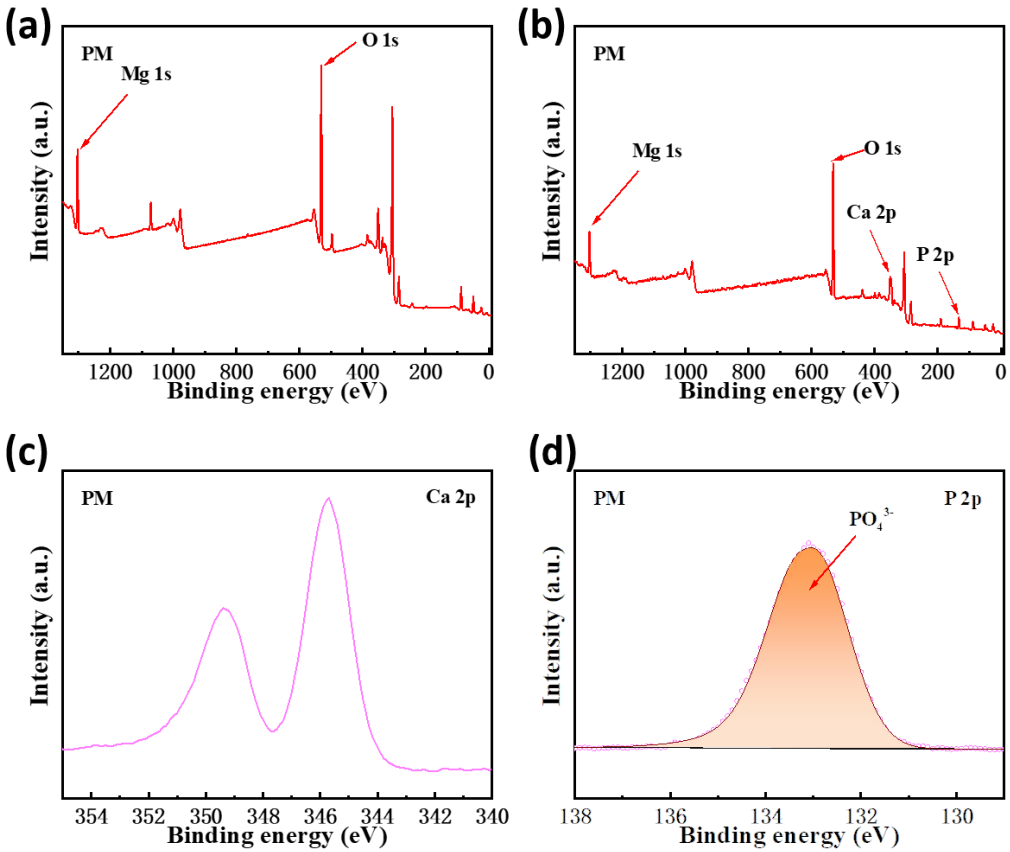

Fig. S3. XPS spectra: (a) Survey spectrum in NaCl solution; (c) Survey spectrum in SBF; (d) Ca 2*p* in SBF; (e) P 2*p* in SBF

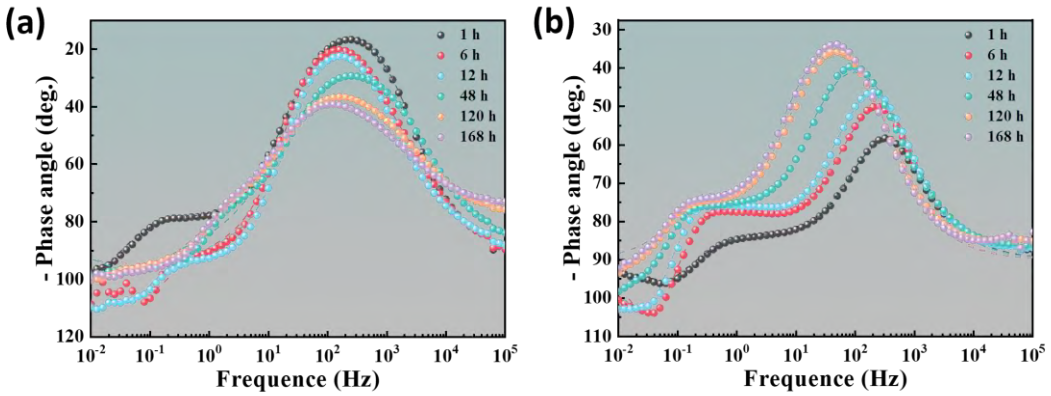

Fig. S4. Bode phase plots of pure Mg in the (a) NaCl solution and (b) SBF

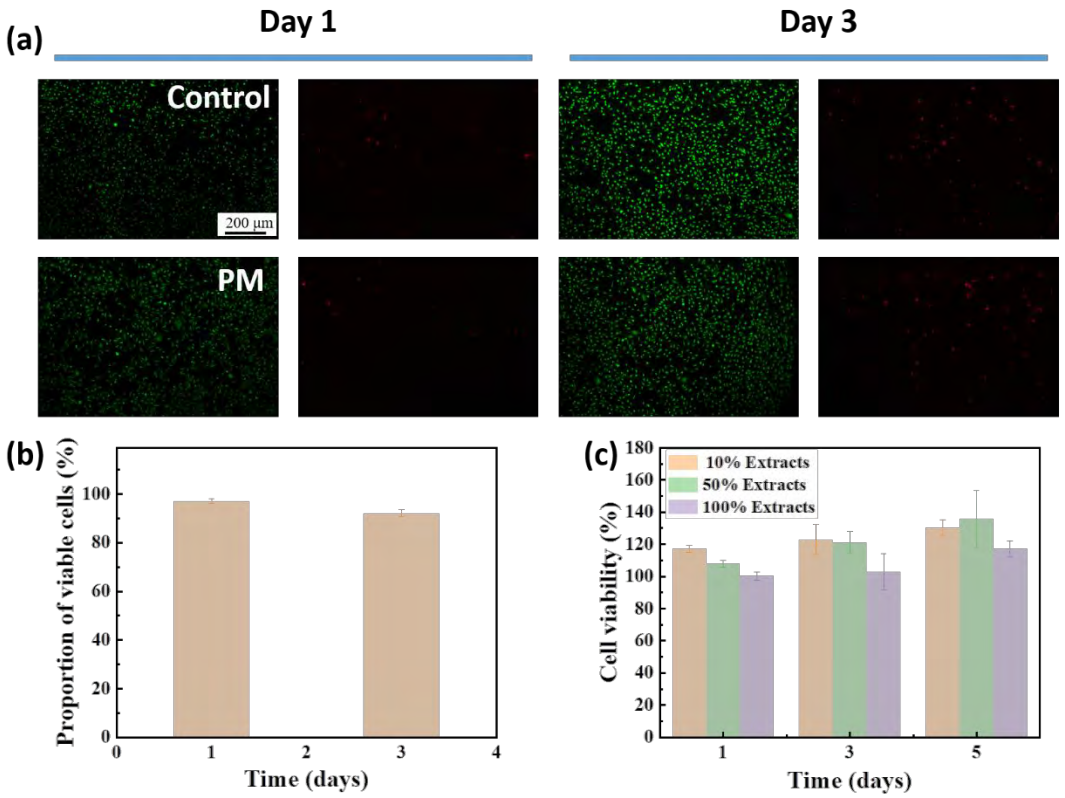

Fig. S5. Evaluation of cytotoxicity and bioactivity of pure magnesium: (a) Live/dead cell staining; (b) Proportions of viable cells; (c) Cell viability.

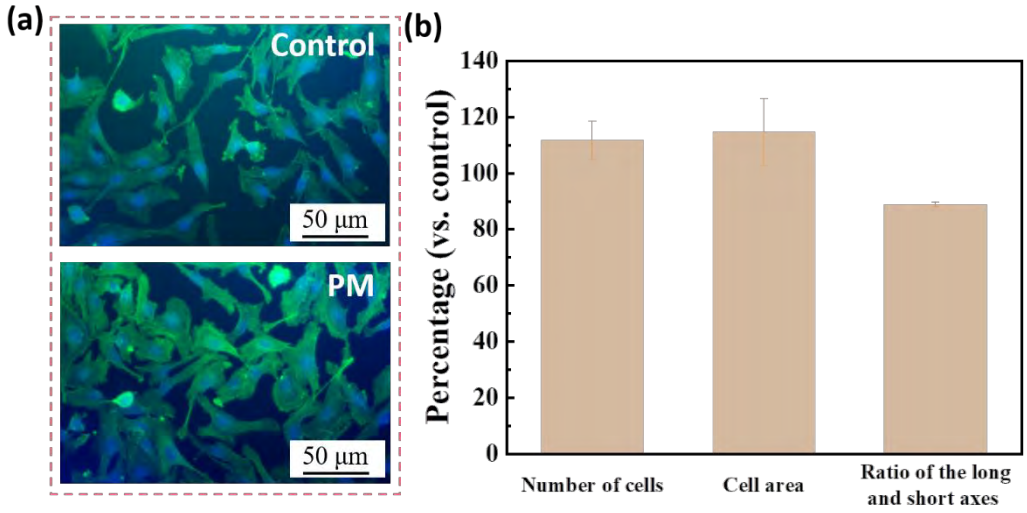

Fig. S6. Evaluation of cell growth in pure magnesium extract: (a) Cell morphology; (b) Number of cells, cell area, and ratio of the long and short axes.